



# MIT Open Access Articles

## *Achieving high-precision pointing on ExoplanetSat: Initial feasibility analysis*

The MIT Faculty has made this article openly available. **Please share** how this access benefits you. Your story matters.

<b>Citation</b>	Christopher M. Pong, Sungyung Lim, Matthew W. Smith, David W. Miller, Jesus S. Villaseñor and Sara Seager, "Achieving high-precision pointing on ExoplanetSat: initial feasibility analysis", Proc. SPIE 7731, 77311V (2010); doi:10.1117/12.857992 © 2010 COPYRIGHT SPIE
<b>As Published</b>	<a href="http://dx.doi.org/10.1117/12.857992">http://dx.doi.org/10.1117/12.857992</a>
<b>Publisher</b>	SPIE
<b>Version</b>	Final published version
<b>Citable link</b>	<a href="http://hdl.handle.net/1721.1/60940">http://hdl.handle.net/1721.1/60940</a>
<b>Terms of Use</b>	Article is made available in accordance with the publisher's policy and may be subject to US copyright law. Please refer to the publisher's site for terms of use.



Massachusetts Institute of Technology

DSpace@MIT

# Achieving high-precision pointing on ExoplanetSat: Initial feasibility analysis

Christopher M. Pong<sup>a</sup>, Sungyung Lim<sup>b</sup>, Matthew W. Smith<sup>a</sup>, David W. Miller<sup>a</sup>,  
Jesus S. Villaseñor<sup>a</sup>, and Sara Seager<sup>a</sup>

<sup>a</sup>Massachusetts Institute of Technology, 77 Massachusetts Ave., Cambridge, MA 02139, USA;  
<sup>b</sup>The Charles Stark Draper Laboratory, 555 Technology Square, Cambridge, MA 02139, USA

## ABSTRACT

ExoplanetSat is a proposed three-unit CubeSat designed to detect down to Earth-sized exoplanets in an orbit out to the habitable zone of Sun-like stars via the transit method. To achieve the required photometric precision to make these measurements, the target star must remain within the same fraction of a pixel, which is equivalent to controlling the pointing of the satellite to the arcsecond level. The satellite will use a two-stage control system: coarse control will be performed by a set of reaction wheels, desaturated by magnetic torque coils, and fine control will be performed by a piezoelectric translation stage. Since no satellite of this size has previously demonstrated this high level of pointing precision, a simulation has been developed to prove the feasibility of realizing such a system.

The current baseline simulation has demonstrated the ability to hold the target star to within 0.05 pixels or 1.8 arcseconds (with an 85 mm lens and 15  $\mu\text{m}$  pixels), in the presence of large reaction wheel disturbances as well as external environmental disturbances. This meets the current requirement of holding the target star to 0.14 pixels or 5.0 arcseconds. Other high-risk aspects of the design have been analyzed such as the effect of changing the guide star centroiding error, changing the CMOS sampling frequency, and reaction wheel selection on the slew performance of the satellite. While these results are promising as an initial feasibility analysis, further model improvements and hardware-in-the-loop tests are currently underway.

**Keywords:** exoplanet, CubeSat, attitude determination and control, staged control, jitter analysis, modeling and simulation

## 1. INTRODUCTION

ExoplanetSat is a concept for a  $10 \times 10 \times 34$  cm three-unit (3U) CubeSat designed to detect extrasolar planets (exoplanets) using the transit method. If an exoplanet's orbital plane is aligned with the line of sight from Earth, the exoplanet will transit in front of the star causing the overall brightness of its star to dim. Observations of these transit events will provide information on the exoplanet's radius and orbital period. The orbital period determines whether the exoplanet resides in the habitable zone of its star, a region where liquid water can exist on the exoplanet's surface. Detection of these exoplanets will enable other observatories to perform follow-up measurements such as Doppler spectroscopy to determine the exoplanet's mass and atmospheric spectroscopy to determine the composition of the exoplanet's atmosphere. All of these pieces of information form the stepping stones to determining if life exists outside of our solar system.

These follow-up measurements, however, are only feasible to perform on exoplanets orbiting bright stars. NASA's Kepler, a satellite launched in March 2009, has a mission to provide a census of exoplanets. To observe enough stars (approximately 150,000), Kepler is imaging a field of faint stars. While this will provide valuable information on the frequency of Earth-sized exoplanets orbiting Sun-like stars, follow-up doppler and atmospheric spectroscopy measurements are not currently feasible for low-mass exoplanets around most of these faint stars. Due to the sparse distribution of bright stars across the sky and the low probability of necessary orbital plane alignment, the discovery of Earth-sized exoplanets orbiting these bright stars will rely on dedicated, inexpensive missions continually monitoring a single target. By adhering to the CubeSat standard, ExoplanetSat can fill this

---

Send correspondence to Christopher Pong: cpong@mit.edu

need and become an inexpensive platform with multiple launch opportunities. It is envisioned that a constellation of ExoplanetSats, each with a different target star, will enable the possibility of detecting down to an Earth-sized exoplanet in an orbit out to the habitable zone of these bright stars.

There are many challenges associated with obtaining the photometric precision required to detect Earth-sized exoplanets. This paper will focus on the satellite's pointing precision and the disturbances that affect the ability to point the satellite. Since no satellite of this size has previously demonstrated the required level of pointing precision, extensive analyses have been performed to determine the feasibility of realizing this system.

A brief overview of the satellite is provided in Section 2 including the attitude determination and control subsystem (ADCS) and concept of operations. Section 3 follows this by describing the simulation and models that were developed to analyze the feasibility of achieving this high-precision pointing. Results from this model are presented in Section 4 and conclusions and planned future work including further hardware testing are given in Section 5.

## 2. BASELINE SATELLITE DESIGN

An overview of the proposed baseline satellite design, with an emphasis on the attitude determination and control subsystem, is provided in this section. One of the potential layouts of some of the important pieces of hardware is shown in Figures 1 and 2. A brief summary of some of the relevant satellite subsystems is given below.

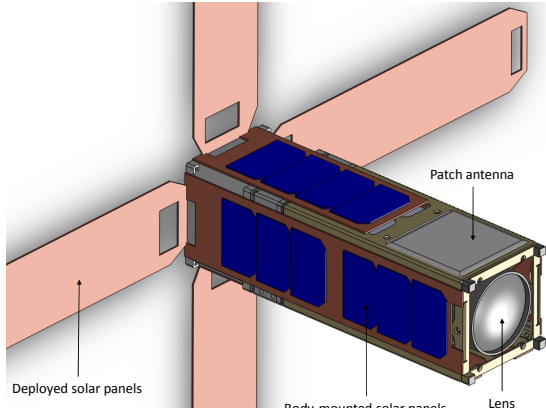


Figure 1: Current design of ExoplanetSat with deployed solar panels.

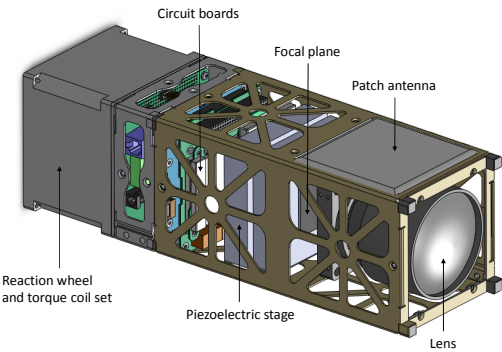


Figure 2: Current layout of components inside the ExoplanetSat structure.

- **Payload:** The main payload is an 85 mm lens and a hybrid focal plane consisting of a CCD to gather light from the target star, with comounted CMOS detectors to image guide stars for attitude determination.
- **Avionics:** A 32-bit microcontroller, FPGA, SDRAM and flash memory form the avionics subsystem. The FPGA is dedicated to processing the CCD and CMOS images while the microcontroller handles all other processes including the ADCS estimation and control loops.
- **Communication:** An S-band transceiver with an omnidirectional antenna and a patch antenna will provide the communication link to the HETE ground stations in Kwajalein, Cayenne, and Singapore.
- **Power:** Four deployed solar panels and additional body-mounted solar panels provide up to 30 W of power to the satellite. During orbit day, energy will be stored in lithium ion/polymer batteries for use during eclipse.
- **Structure:** An off-the-shelf chassis will be modified to provide the structure to hold all of the components within the  $10 \times 10 \times 34$  cm volume. The current total mass is approximately 5 kg.

- **Thermal:** Passive thermal isolation and cooling of the CCD and CMOS detectors and thermal control of the other components are provided by surface finishes/coatings as well as multi-layer insulation (MLI). Temperatures are monitored with small analog temperature sensors located throughout the satellite.

More details on these subsystems can be found in Smith et al.<sup>1</sup>

## 2.1 Attitude determination and control subsystem (ADCS)

To achieve the photometric precision required to detect Earth-sized exoplanets, the target star must remain on the same position on the detector to within a fraction of a pixel. This stems from the fact that the CCD response changes both within and between pixels. Movement of the star on the CCD, even less than a pixel, can cause enough variation of measured photons to mask the signature of Earth-sized exoplanets. Based off of the analyses presented in Smith et al.,<sup>1</sup> a requirement of restricting the target star motion to 0.14 pixels ( $3\sigma$ ) or 5.0 arcseconds in the cross-boresight attitude axes ( $3\sigma$ ), was developed. This jitter level directly corresponds to a noise level of the measured brightness of the target star and therefore the detectable size of any transiting exoplanets. If this requirement can be met, the analyses show that Earth-sized exoplanets can be detected around stars down to 4<sup>th</sup> magnitude. A large margin has been included when developing this requirement to account for unmodeled effects such as intrapixel variation.

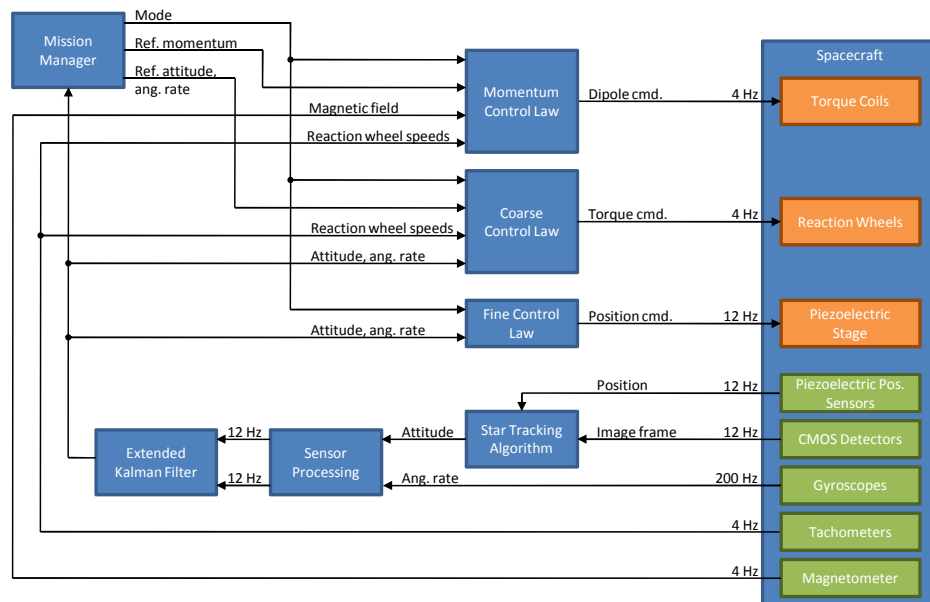


Figure 3: Block diagram of the attitude determination and control subsystem on ExoplanetSat.

To maximize pointing precision, the ADCS employs a staged control approach. Reaction wheels provide coarse control down to a certain deadband while torque coils desaturate the reaction wheels periodically. Fine control is provided by a piezoelectric stage, which translates the focal plane (orthogonal to the boresight axis) to stabilize the image further. Figure 3 shows a detailed block diagram of this subsystem. The CMOS detectors are used to image the guide stars around the target star, which are then centroided, corrected by the piezoelectric position sensors, and matched against a star catalog to determine the satellite's attitude. Gyroscope measurements provide information on the satellite's angular rate. These measurements are filtered and downsampled to match the rate of the CMOS detectors. In addition, processing delays from the attitude measurements of the CMOS detectors are compensated. Both the gyroscope and CMOS detector attitude measurements are then combined in an extended Kalman filter. Additional sensors such as coarse sun sensors (from the solar panels) and the magnetometer can provide redundant attitude determination capabilities, if needed. Guidance is provided by a mission manager that calculates the current mode as well as reference commands to the various controllers.

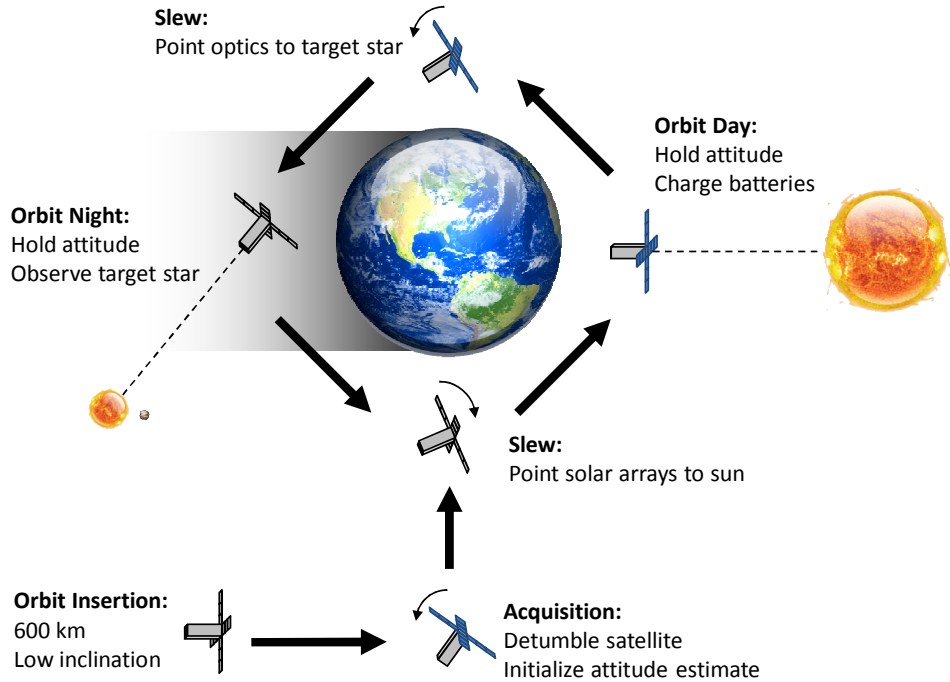


Figure 4: Nominal modes of operation on ExoplanetSat.

## 2.2 Concept of operations

Figure 4 shows the baseline control modes that outline the concept of operations for ExoplanetSat. The ideal orbit that the satellite will be injected into is a 600 km circular, equatorial orbit. This allows the satellite to operate in an environment with low radiation, avoiding the harsh regions of the Van Allen radiation belts and the South Atlantic Anomaly. In addition, the high altitude reduces the effect of aerodynamic drag on the satellite, which would cause unwanted disturbance torques. This orbit, while ideal, will likely change depending on available launch opportunities.

Upon release from the launch vehicle, the satellite deploys its solar arrays and begins its operations in acquisition mode. Note that the CubeSat standard allows the satellite to be launched with charged batteries,<sup>2</sup> enabling the satellite to begin operations based only upon launch vehicle restrictions. In acquisition mode, the satellite reduces its angular rate using torque coils and initializes its attitude estimate with the on-board sensors. Once the satellite has reduced the angular rates enough for the reaction wheels to capture the satellite, it slews such that its solar panels face the sun. Nominal operations begin once the batteries are fully charged.

During nominal operations, the satellite slews when entering and exiting eclipse, twice per orbit. During orbit day, the satellite points its solar panels to the sun to charge the batteries. During orbit night, the satellite observes the target star. Alpha Centauri B will serve as the selected target star in this paper since it is a top candidate for the first ExoplanetSat mission. Its bright apparent magnitude, favorable orbital period for exoplanets in the habitable zone, and large inclination suitable for year-round observation make it an attractive target star.

## 3. SATELLITE SIMULATION & MODELS

The feasibility analysis up to this point has focused on the development of a high-fidelity simulation of the satellite. One of the major design choices was whether to develop a frequency-domain simulation or a time-domain simulation. The attraction of a frequency-domain simulation is in its simplicity. Given power spectral densities (PSDs) of the inputs (e.g., reaction wheel disturbances), PSDs of output variables of interest (e.g.,

position of the star on the CCD), can be calculated with the following equation<sup>3</sup>

$$\Phi_z = \mathbf{G}(j\omega)\Phi_u\mathbf{G}^H(j\omega) \quad (1)$$

where  $\Phi_u$  is the input PSD matrix,  $\Phi_z$  is the output PSD matrix,  $\mathbf{G}(j\omega)$  is the transfer function matrix of the satellite, and  $^H$  denotes the conjugate transpose operation. The output PSDs can then be integrated over all frequencies to provide the mean-square value of the outputs, which can be converted into  $3\sigma$  deviations. This procedure allows for direct computation of steady-state deviations by linearizing the closed-loop equations of motion (which can be performed automatically, e.g., by MATLAB's Symbolic Math Toolbox) followed by simple matrix multiplications. The problem with this analysis is that it cannot handle transient behavior (slew maneuvers, Kalman filter gains), nonlinear behavior (quantized, discretized and saturated actuator commands and sensor outputs) and multiple rates (continuous dynamics mixed with discrete computation). Due to the stringent requirements, it was decided that the time-domain simulation was the better choice to provide more accurate results. Using the time-domain simulation, however, comes at the cost of a larger computational load, which can be an issue when iterating over many design choices.

Nonlinear time-domain models including models of the satellite dynamics, actuators, sensors and software are provided in the sections below. The simulation was implemented in MATLAB/Simulink and is based heavily from previously developed Simulink models.<sup>4</sup>

### 3.1 Attitude dynamics

The attitude of the satellite is defined as the rotation from the body frame,  $\mathcal{F}_B$ , to the inertial frame,  $\mathcal{F}_I$ . This rotation can be represented as a quaternion, a four-element vector defined as

$$\mathbf{q} = [q_0 \quad q_1 \quad q_2 \quad q_3]^T = [q_0 \quad \mathbf{q}_{13}]^T \triangleq [\cos \frac{\theta}{2} \quad \mathbf{a} \sin \frac{\theta}{2}]^T \quad (2)$$

where  $\mathbf{a}$  is the eigenaxis and  $\theta$  is the angle of rotation about the eigenaxis that defines the rotation from  $\mathcal{F}_B$  to  $\mathcal{F}_I$ . The angular rate of the satellite,  $\boldsymbol{\omega} = [\omega_1 \quad \omega_2 \quad \omega_3]^T$ , is defined as the angular rate of  $\mathcal{F}_B$  with respect to  $\mathcal{F}_I$ , expressed in  $\mathcal{F}_B$ . With these definitions, the rigid-body kinematic and kinetic equations of motion are

$$\dot{\mathbf{q}} = \frac{1}{2}\boldsymbol{\Omega}(\boldsymbol{\omega})\mathbf{q} = \frac{1}{2} \begin{bmatrix} 0 & \omega_1 & \omega_2 & \omega_3 \\ -\omega_1 & 0 & \omega_3 & -\omega_2 \\ -\omega_2 & -\omega_3 & 0 & \omega_1 \\ -\omega_3 & \omega_2 & -\omega_1 & 0 \end{bmatrix} \mathbf{q} \quad (3)$$

and

$$\dot{\boldsymbol{\omega}} = \mathbf{J}^{-1}(-\boldsymbol{\omega} \times (\mathbf{J}\boldsymbol{\omega} + \mathbf{h}_{RW}) + \boldsymbol{\tau}) \quad (4)$$

where  $\mathbf{J}$  is the moment of inertia about the center of mass of the satellite in  $\mathcal{F}_B$ ,  $\mathbf{h}_{RW}$  is the momentum of the reaction wheels in  $\mathcal{F}_B$ <sup>\*</sup>, and  $\boldsymbol{\tau}$  is the sum of all control and disturbance torques acting on the satellite in  $\mathcal{F}_B$ . To relax the assumption of satellite rigidity, the equations of motion can be modified to include structural flexibility. A simple approach, derived from Sidi,<sup>5</sup> is to define a transfer function that takes in the angular acceleration of a single axis of the satellite,  $\alpha$ , and outputs the angular rate of the satellite due to the  $i^{th}$  flexible mode,  $\omega_{flex,i}$ :

$$\frac{\omega_{flex,i}(s)}{\alpha(s)} = \frac{2^{J_a/J_o}s}{s^2 + 2\zeta\omega_n s + \omega_n^2} \quad (5)$$

where  $s$  is the Laplace variable,  $J_a$  is the inertia of the flexible appendage,  $J_o$  is the inertia of the satellite bus,  $\zeta$  is the damping of the flexible mode (typically very low, on the order of 0.001), and  $\omega_n$  is the natural frequency of the flexible mode. Multiple modes about various axes, including cross coupling of axes, can either be estimated for preliminary designs or determined with software packages such as NASTRAN. These modes are combined to produce the three-axis angular rate of the satellite due to flexibility, which is added to the angular rate of the satellite determined by integrating Equation 4. This total angular rate can then be integrated with Equation 3 to determine the attitude of the satellite.

---

\*For a set of three orthogonal reaction wheels aligned to the body axes,  $\mathbf{h}_{RW} = \mathbf{J}_{RW}\boldsymbol{\omega}_{RW}$  where  $\mathbf{J}_{RW}$  is a diagonal matrix of the reaction wheel inertias about the spin axis and  $\boldsymbol{\omega}_{RW}$  is a vector of the reaction wheel speeds.

### 3.2 Orbital dynamics and environmental disturbances

The orbit of the satellite around Earth is simulated to give an accurate representation of the space environment. The position,  $\mathbf{r}$ , and velocity,  $\mathbf{v}$ , of the satellite in the Earth-centered inertial frame is determined by solving Kepler's problem given the classical orbital elements and simulation time as described by Vallado.<sup>6</sup> These are fed into a module that determines the disturbance torques acting on the satellite: gravity gradient, magnetic, aerodynamic and solar.

Torques caused by the gravity gradient across the satellite can be calculated as<sup>7</sup>

$$\boldsymbol{\tau}_{gg} = \frac{3\mu}{r^3} (\hat{\mathbf{r}} \times \mathbf{J}\hat{\mathbf{r}}) \quad (6)$$

where  $\mu$  is the Earth's gravitational constant,  $r = \sqrt{\mathbf{r}^T \mathbf{r}}$ , and  $\hat{\mathbf{r}}$  is the normalized position of the satellite in  $\mathcal{F}_B$ .

Magnetic disturbance torques are created by the interaction of satellite's residual magnetic dipole as well as the dipole created by the torque coils with the Earth's magnetic field. This torque can be calculated as<sup>7</sup>

$$\boldsymbol{\tau}_{mag} = \mathbf{m}_{tot} \times \mathbf{b} \quad (7)$$

where  $\mathbf{m}_{tot}$  is the total magnetic dipole in  $\mathcal{F}_B$  and  $\mathbf{b}$  is the local magnetic field of Earth in  $\mathcal{F}_B$ . The magnetic field model used in the simulation is a dipole model of Earth,<sup>8</sup> using the first-degree 2010 coefficients<sup>9</sup> from the 11<sup>th</sup> Generation International Geomagnetic Reference Field (IGRF). Higher fidelity models such as the complete IGRF model or the World Magnetic Model (WMM) were not used due to their higher computational load.

Aerodynamic drag from the thin atmosphere causes torques due to the offset of the center of pressure and center of mass of the satellite. The aerodynamic force on the  $i^{th}$  satellite face is<sup>7</sup>

$$\mathbf{f}_i = -\frac{1}{2} c_{drag} \rho v^2 a_i (\hat{\mathbf{n}}_i \cdot \hat{\mathbf{v}}) \hat{\mathbf{v}} \quad (8)$$

where  $c_{drag}$  is the drag coefficient (typically around 2.5),  $\rho$  is the atmospheric density,  $a_i$  is the  $i^{th}$ -face surface area,  $\hat{\mathbf{n}}_i$  is the  $i^{th}$ -face surface normal in  $\mathcal{F}_B$ ,  $v = \sqrt{\mathbf{v}^T \mathbf{v}}$ , and  $\hat{\mathbf{v}}$  is the normalized satellite velocity in  $\mathcal{F}_B$ . The atmospheric density is calculated from the U.S. Standard Atmosphere 1976 model<sup>10</sup> and held constant throughout the simulation, assuming a circular orbit. The aerodynamic torque can then be calculated summing the contributions of each face,

$$\boldsymbol{\tau}_{aero} = \sum_{i \in \mathcal{I}} (\mathbf{l}_i \times \mathbf{f}_i) \quad (9)$$

where  $\mathbf{l}_i$  is the  $i^{th}$ -face lever arm and  $\mathcal{I}$  is the set of all satellite faces for which  $\hat{\mathbf{n}}_i \cdot \hat{\mathbf{v}} > 0$ .

When the satellite is in sunlight, the solar flux induces a force on the satellite. This force on the  $i^{th}$  face is<sup>7</sup>

$$\mathbf{f}_i = -\frac{F_s a_i}{c} (\hat{\mathbf{n}}_i \cdot \hat{\mathbf{s}}) \left[ (1 - c_{spec}) \hat{\mathbf{s}} + 2(c_{spec} (\hat{\mathbf{n}}_i \cdot \hat{\mathbf{s}}) + \frac{1}{3} c_{diff}) \hat{\mathbf{n}} \right] \quad (10)$$

where  $F_s = 1367 \text{ W/m}^2$  is the solar constant,  $c = 3 \times 10^8 \text{ m/s}$  is the speed of light,  $c_{spec}$  and  $c_{diff}$  are the specular and diffuse reflection coefficients,  $\hat{\mathbf{s}}$  is the normalized position of the sun in  $\mathcal{F}_B$  relative to the satellite,  $a_i$  is the  $i^{th}$ -face surface area, and  $\hat{\mathbf{n}}_i$  is the  $i^{th}$ -face surface normal in  $\mathcal{F}_B$ . The solar torque can then be calculated summing the contributions of each face,

$$\boldsymbol{\tau}_{solar} = \sum_{i \in \mathcal{I}} (\mathbf{l}_i \times \mathbf{f}_i) \quad (11)$$

where  $\mathbf{l}_i$  is the  $i^{th}$ -face lever arm and  $\mathcal{I}$  is the set of all satellite faces for which  $\hat{\mathbf{n}}_i \cdot \hat{\mathbf{s}} > 0$ . Note that both the aerodynamic and solar disturbances are calculated ignoring shadowing of the sun or blocking of the air velocity.

### 3.3 Reaction wheel dynamics and disturbances

In addition to the external disturbances of the space environment there are internal disturbances that arise from the reaction wheels. Modeling of reaction wheels has been an active area of research<sup>11–14</sup> since the induced vibrations of these assemblies are often the largest source of satellite jitter. Tonal disturbances (both forces and torques) tied to the reaction wheel speed are modeled as sinusoids,

$$m_i(t) = c_i \omega_{RW}^2 \sin(h_i \theta_{RW}(t) + \phi_i) \quad (12)$$

where  $c_i$  is the coefficient of the  $i^{th}$  harmonic,  $h_i$  is the harmonic number of the  $i^{th}$  harmonic,  $\omega_{RW}$  is the speed of the reaction wheel,  $\theta_{RW}$  is the phase of the reaction wheel, and  $\phi_i$  is a uniformly distributed random variable over the domain  $[0, 2\pi]$ . Each reaction wheel produces radial disturbances (forces and torques orthogonal to the spin axis) that are offset by  $90^\circ$  in phase between the two axes as well as axial disturbances (forces and torques in the direction of the spin axis) for each of the harmonics. The harmonics and their corresponding coefficients are wheel-dependent and are therefore determined experimentally. This modeling technique has been validated<sup>13, 14</sup> by showing that this model captures the same power content as the measured vibrations.

### 3.4 Piezoelectric stage dynamics

The piezoelectric stage is currently modeled as a linear, second-order, *closed-loop* system whose input is the commanded position,  $x_{cmd}$ , and output is the actual position,  $x_{act}$ . The transfer function is given by

$$\frac{x_{act}(s)}{x_{cmd}(s)} = \frac{\omega_n^2}{s^2 + 2\zeta\omega_n s + \omega_n^2} \quad (13)$$

where  $\zeta$  is the closed-loop damping and  $\omega_n$  is the closed-loop bandwidth of the piezoelectric stage. Since the piezoelectric stage is being custom built and the internal controller gains can be tuned, these parameters are constrained by mass, volume and power considerations. The closed-loop bandwidth can be set up to an order of magnitude less than the sampling rate of the internal piezoelectric stage control loop. The bandwidth is currently set to 10 Hz, allowing for low sampling rates of the piezoelectric stage on the order of 100 Hz, while achieving reasonable settling times (e.g., 70 ms with  $\zeta = 0.995$ ). This model can be improved in the future by developing a nonlinear, open-loop model of the piezoelectric stage dynamics and closing the loop with a proportional-integral-derivative (PID) controller.

### 3.5 Optics model

A simple pinhole optics model is currently used in the simulation. The star's unit vector in the inertial frame can be calculated from the star's right ascension and declination and transformed into the focal-plane frame, knowing the satellite's attitude. This unit vector,  $r_{star} = [x \ y \ z]^T$ , along with the focal length of the lens,  $f$ , can be used to calculate the position of the star on the focal plane,  $[u \ v]^T$ :

$$u = f \frac{x}{z} \quad (14a)$$

$$v = f \frac{y}{z}. \quad (14b)$$

To determine the position of the star on the CCD, the position of the piezoelectric stage is simply subtracted out. This is the main figure of merit for the simulation: the motion of the target star on the CCD. This can be converted to pixels by dividing the size of a pixel.

In addition to imaging the target star on the CCD, the CMOS detectors provide images of guide stars to serve as a star tracker. The actual star tracking algorithms have not yet been incorporated into the simulation. Instead, it is assumed that the CMOS detectors can provide attitude information plus white Gaussian noise. The attitude error due to this noise can be estimated as<sup>15</sup>

$$\sigma_{cross-boresight} = \frac{a \sigma_{centroid}}{n_{pix} \sqrt{n_{star}}} \quad (15a)$$

$$\sigma_{boresight} = \arctan\left(\frac{\sigma_{centroid}}{0.3825n_{pix}}\right) \frac{1}{\sqrt{n_{star}}} \quad (15b)$$

where  $a$  is the field of view,  $n_{pix}$  is the number of pixels across the detector,  $n_{star}$  is the number of centroided stars, and  $\sigma_{centroid}$  is the error in the centroid of the stars. Since most star trackers can only operate when the angular rates are low, these attitude measurements are disabled when the satellite is rotating too fast.

### 3.6 Gyroscope model

The gyroscopes measure the angular rate of the satellite. The main noise sources of gyroscopes that are modeled are angle random walk and bias instability. A simple model<sup>16</sup> of the gyroscope output that includes these noise terms is

$$\mathbf{y} = \boldsymbol{\omega} + \mathbf{b} + \mathbf{v}_1 \quad (16)$$

where  $\mathbf{b}$  is the gyroscope biases, which follow the dynamics

$$\dot{\mathbf{b}} = -\frac{\mathbf{b}}{\tau} + \mathbf{v}_2, \quad (17)$$

$\tau$  is the bias stability time constant,  $\mathbf{v}_1$  is a zero-mean, Gaussian white-noise process that causes angle random walk, and  $\mathbf{v}_2$  is a zero-mean, Gaussian white-noise process that drives the instability of the biases.

### 3.7 Software: Guidance

The mission manager is a simple, preprogrammed timeline of control mode transitions as well as reference attitude and reaction wheel momentum instructions. For slew maneuvers, these are inputs into a slew command generator that calculates a spinup-coast-spindown slew profile and outputs the appropriate reference attitude quaternion and angular rate during the slew. Reaction wheel momentum is commanded to keep the reaction wheels within a desired range during orbit night. This mitigates any potential coupling between the disturbances produced by the reaction wheels and flexible modes of the satellite.

### 3.8 Software: Navigation

The satellite is able to estimate its attitude and angular rates based off of outputs from the CMOS detectors as well as the gyroscopes. These sensor outputs are combined in an extended Kalman filter (EKF) with a body-fixed covariance representation described by Lefferts, Markley and Shuster.<sup>16</sup> Complete equations for this filter are omitted for brevity.

During orbit night, the CMOS detectors act as a star tracker. This sensor output along with the gyroscopes are combined in the EKF. This EKF estimates the vector part of the attitude error quaternion along with the gyroscope biases. During slew maneuvers and orbit day, the CMOS detectors will not be used and the attitude will be estimated by directly integrating the gyroscopes. Estimated gyroscope biases are held constant during this time. The estimates of the attitude error along with the gyroscope biases are used to formulate the satellite's attitude quaternion and angular rate.

### 3.9 Software: Control

Coarse attitude control is provided by a simple, yet effective nonlinear proportional-derivative (PD) controller based off the controller presented by Wie.<sup>17</sup> This control torque commands that are distributed among the reaction wheels is given by

$$\tau_{RW} = -2\omega_n^2 \mathbf{J} \mathbf{q}_{e13} - 2\zeta\omega_n \mathbf{J} \boldsymbol{\omega}_e - \mathbf{m}_{MT} \times \mathbf{b} + \boldsymbol{\omega} \times (\mathbf{J} \boldsymbol{\omega} + \mathbf{h}_{RW}) \quad (18)$$

where  $\zeta$  is the closed-loop damping,  $\omega_n$  is the closed-loop bandwidth,  $\mathbf{J}$  is the estimated satellite inertia (not necessarily the same as the actual satellite inertia),  $\mathbf{q}_{e13}$  is the vector part of the error quaternion defining the rotation from the reference quaternion to the current quaternion,  $\mathbf{q}_r$ , given by

$$\mathbf{q}_e = \begin{bmatrix} q_{c0}q_{r0} + \mathbf{q}_{c13} \cdot \mathbf{q}_{r13} \\ q_{c0}\mathbf{q}_{r13} - q_{r0}\mathbf{q}_{c13} + \mathbf{q}_{c13} \times \mathbf{q}_{r13} \end{bmatrix}, \quad (19)$$

$\omega_e$  is the error between the reference angular rate,  $\omega_r$ , and the current angular rate,  $\mathbf{m}_{MT}$  is the commanded magnetic dipole in  $\mathcal{F}_B$ , and  $\mathbf{b}$  is the measured magnetic field in  $\mathcal{F}_B$ . The first two terms of Equation 18 are the proportional and derivative terms, while the last two terms are computed torques to cancel out the nonlinearities of Equation 4. The closed-loop damping is typically set to  $\zeta = 0.995$  for a fast settling time of pointing and tracking systems. The closed-loop bandwidth is set to 100 times slower than the controller sampling rate for a conservative frequency separation between the controller sampling rate, any anti-aliasing filters in the feedback loop, and the closed-loop bandwidth.

The magnetic torque coils are actuated to control the momentum of the reaction wheels using the momentum projection method described in Sidi.<sup>5</sup> Momentum control is active only during orbit day to conserve energy during orbit night.

The piezoelectric stage is commanded to move based on the output of the CMOS detectors. The position command is simply a calculation of the target star position on the focal plane based on the current attitude estimate from the EKF.

#### 4. DATA, RESULTS, & ANALYSIS

The model described in Section 3 can be used to analyze the satellite's performance with many different hardware options, software parameters, as well as mission scenarios. One of the main trade studies that was analyzed with this model is the selection of the reaction wheels. The four options analyzed in this paper are given in Table 1.

Table 1: Reaction wheel specifications.

Company	Model	Wheel Inertia [kg·m <sup>2</sup> · 10 <sup>-6</sup> ]	Max. Wheel Speed [rpm]	Mtm. Storage [mN·m·s]	Max. Torque [mN·m]
Maryland Aerospace, Inc.	MAI-100 <sup>18</sup>	10.35	1,000	1.1	0.635
	MAI-200 <sup>19</sup>	10.35	10,000	10.8	0.635
Astro- und Feinwerktechnik Adlershof GmbH <sup>20</sup>	RW 1 Type A	0.6945	16,380	1.2	0.023
	RW 1 Type B	0.1195	16,380	0.2	0.004

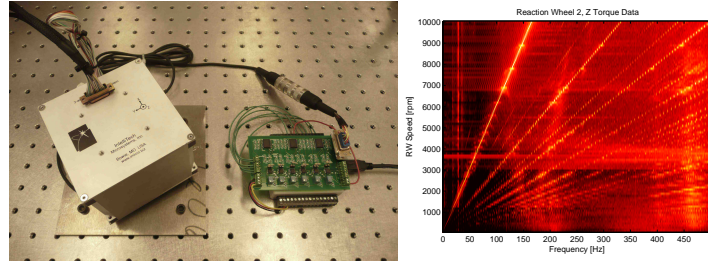
In addition to this trade study, the model was used to analyze the aspects of the design with the highest risk. This includes the vibrations produced by the reaction wheels due to imbalances, the precision of the centroiding algorithm used in the star tracking algorithms for attitude determination, and the sampling frequency of the CMOS detectors. The selection of the reaction wheel disturbance parameters is discussed in Section 4.1. The other important parameters used for the baseline case are given in Section A.

This is followed by a jitter analysis of the achievable pointing precision in Section 4.2 and a slew analysis in Section 4.3 to demonstrate the feasibility of creating a satellite that can achieve high pointing precision every during every orbit night.

##### 4.1 Reaction wheel disturbances

As mentioned in Section 3.3, each reaction wheel has a unique set of tonal disturbances. Therefore, to ensure adequate on-orbit performance, each reaction wheel's disturbance characteristics must be measured. Initial tests on the MAI-200 have been performed at the Massachusetts Institute of Technology Space Systems Laboratory (SSL). Figure 5a shows the MAI-200 mounted on a force/torque sensor with the signal conditioning and data acquisition circuitry. Figure 5a shows a sample of the data produced by this testing. The reaction wheel was run at a set of discrete speeds up to the maximum wheel speed. These time-domain data sets were converted to PSDs and plotted as a waterfall plot. The radial spokes coming out the origin are the tonal disturbances tied to the reaction wheel spin rate. The most dominant disturbance is the fundamental harmonic. These results will be confirmed by further testing at the Kistler Load table in the Goddard Space Flight Center.

For the purposes of this paper, the reaction wheels are assumed to have a static imbalance of 500 mg·mm and a dynamic imbalance of 50,000 mg·mm<sup>2</sup>, which are the coefficients,  $c_i$ , of the fundamental harmonic ( $h_i = 1$ ). Preliminary results from the MAI-200 testing at the SSL indicate that this is a large overestimate of the actual



(a) MAI-200 test setup. (b) MAI-200 waterfall plot.  
Figure 5: Test setup and sample data for the MAI-200 taken at the SSL.

imbalances of the wheels. Also, since the imbalances typically scale with the reaction wheel inertia, the RW 1 wheels are expected to have even smaller imbalances. Other harmonics are not included in this analysis since the harmonic number varies greatly between wheel manufacturers. A final analysis should include these harmonics. However, for this initial feasibility study, only the fundamental harmonics are included.

#### 4.2 Jitter analysis

The simulation was run with the baseline parameters for each of the reaction wheel types. Figure 6 shows the coarse and fine motion of the centroid of the target star on the CCD with the MAI-200. The coarse star motion (piezoelectric stage off) clearly shows a low and a high frequency component of the centroid error. The low frequency component is due to the reaction wheels' inability to control the attitude precisely—the low control bandwidth along with the discretization and quantization of the commanded torques causes the satellite's attitude to drift within a certain deadband. The high frequency, tonal, component is due to the imbalances of the reaction wheels. The fine motion (piezoelectric stage on) shows that most of the low frequency drift is removed. This effect can be seen in Figure 7, where the low frequency components of the coarse PSD of the target star motion are greatly reduced in the fine PSD. The fine target star motion has an additional 12 Hz component and corresponding harmonics due to the discrete commanding of the piezoelectric stage. In addition the 16.7 Hz component from the reaction wheel imbalances are present in the coarse and fine PSDs since the overall system bandwidth is much lower than this disturbance. The piezoelectric stage, therefore cannot compensate for this motion. All of these spikes in the fine PSD, do not contribute greatly to the overall target star motion since the cumulative root mean square (RMS) does not exhibit any step changes at these frequencies. The pointing precision, at this point, is mainly limited by the star tracking attitude determination precision.

This simulation was repeated for all the different reaction wheel types and the results are summarized in Table 2. This table shows that the fine star motion is independent of the reaction wheel selection and that the star motion can be limited to 0.05 pixels or 1.8 arcseconds ( $3\sigma$ ). This fine motion is independent of the reaction wheels because, in each case, the piezoelectric stage is able to remove the low-frequency drift of the reaction wheels down to the error of the estimated attitude. This demonstrated target star motion meets the requirement of bounding the target star motion to within 0.14 pixels or 5.0 arcseconds ( $3\sigma$ ).

Table 2: Jitter performance for the baseline case of various reaction wheels.

Reaction Wheel	Coarse $3\sigma$ Jitter [pixels]	Fine $3\sigma$ Jitter [arcsec]	Coarse $3\sigma$ Jitter [pixels]	Fine $3\sigma$ Jitter [arcsec]
MAI-100	3.0	109	0.05	1.8
MAI-200	1.5	53	0.05	1.8
RW 1 Type A	0.9	32	0.05	1.8
RW 1 Type B	1.2	42	0.05	1.8

This table also shows the pointing precision that can be achieved without the piezoelectric stage, which may be considered for reduced-performance designs. The pointing precision is different between the reaction wheel types due to the angular momentum of the wheels and the quantization of the torque commands. A higher

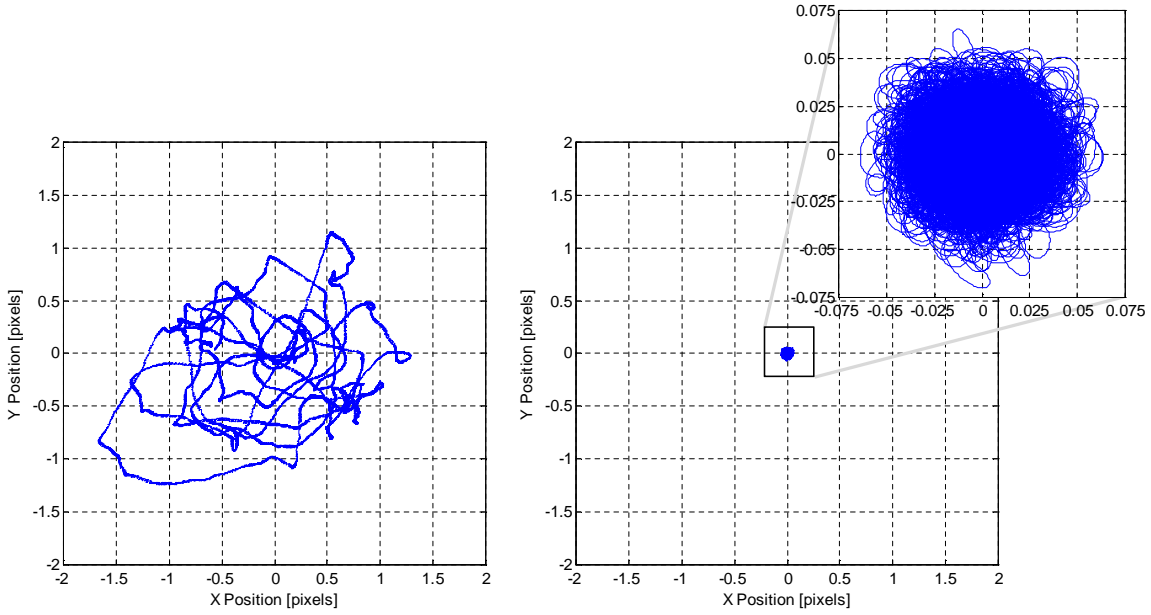


Figure 6: Motion of the target star on the CCD without the piezoelectric stage (left) and with the piezoelectric stage (right) using the MAI-200.

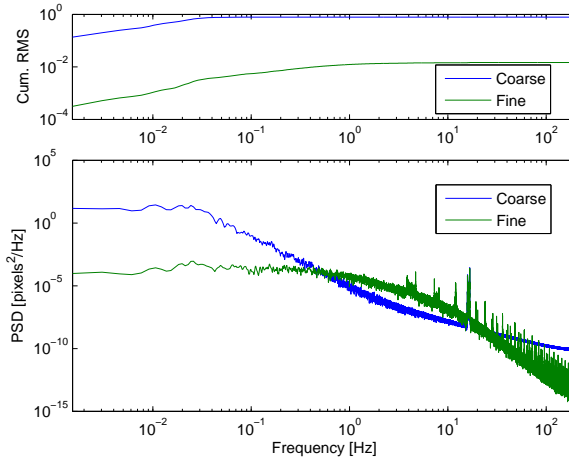


Figure 7: Frequency components of the target star motion with the MAI-200.

angular momentum provides the satellite with additional gyroscopic stiffness, which reduces the target star motion. Note that in this simulation, the reaction wheel nominal speeds are set to 10% of the wheel's maximum speed. This angular momentum difference is the main reason why the MAI-200 and the RW 1 Type A perform better than the MAI-100 and RW 1 Type B, respectively. In addition, the lower torque quantization levels of the RW 1 wheels provide finer torque control versus the MAI wheels allowing the attitude to be held to a tighter bound.

At this point in the analysis, it is unnecessary to analyze the jitter performance at all reaction wheel speeds. Since the reaction wheel disturbances are modeled with a quadratic dependence on reaction wheel speed (Equation 12) and the effect of vibrations on the satellite decreases quadratically with frequency, the two effects cancel, producing the same jitter for all reaction wheel speeds. This will change, however, when multiple disturbance harmonics and accurate flexible modes of the structure are included in the model. The reaction wheels, when run at certain wheel speeds can create disturbances that excite the flexible modes and create large jitter responses.

As an example, if the deployed solar panels have a flexible mode at  $\omega_n = 16.7$  Hz in the cross-boresight axes, with  $\zeta = 0.001$  and  $J_a/J_o = 0.07$ , and the reaction wheels are running at 1000 rpm, the flexible mode will be excited. Figures 8 and 9 shows the resulting target star motion. It is clear that the vibrations of the reaction wheels are amplified and since they are high frequency, the piezoelectric stage cannot counteract this motion. From this example, it is clear that further analysis must be performed to determine the ranges of wheel speeds where the reaction wheels may operate during target star observations based on the harmonics that are present and the flexible modes of the structure.

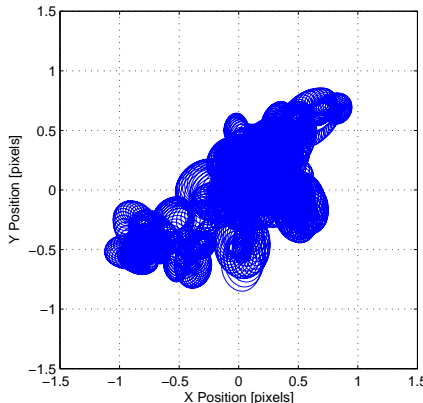


Figure 8: Coarse target star motion when the reaction wheel vibrations excite a flexible mode.

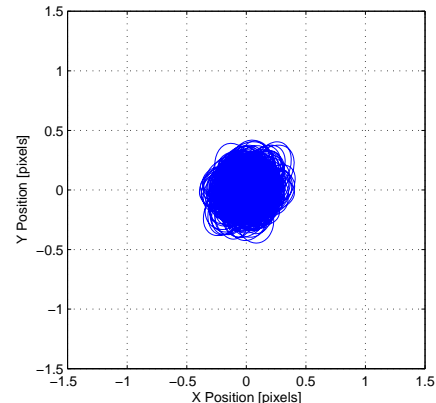


Figure 9: Fine target star motion when the reaction wheel vibrations excite a flexible mode.

Since the pointing precision for the baseline case is limited by the centroiding error, which at this point is a somewhat unknown quantity, it is important to see how the satellite performs as the centroiding error increases. A Monte Carlo simulation was run to determine this relationship. Figure 10 shows that there is a fairly linear relationship with a shallow slope. For the baseline case of a centroiding error of 0.15 pixels ( $3\sigma$ ), the satellite can control the target star motion to around 0.05 pixels ( $3\sigma$ ). This occurs because the centroiding error is averaged over many guide stars in the field of view (10 guide stars gives an error reduction of about a factor of 3), meaning the target star motion is controlled down to the error of the CMOS detectors and algorithms. As the centroiding error increases, this 3:1 ratio no longer holds. For the case of a 1.05 ( $3\sigma$ ) centroiding error, there is a 10:1 ratio of centroiding error to target star motion. This larger ratio is mostly due to the EKF being able to filter out most of this noise by using the internal model of the spacecraft as well as gyroscope measurements. Figure 11 shows this pitch-axis attitude error reduction due to the EKF. These results indicate that the centroiding algorithm does not need to be extremely accurate to control the satellite. Even near the absolute worst-case error of 1 pixel ( $3\sigma$ ), detection of Earth-sized exoplanets should still be possible.

Another high-risk item in the current design is the amount of computations that the avionics will have to perform. The processing of the CMOS images to provide an attitude estimate and the Kalman filter will likely be the most computationally intensive processes. Since it may be necessary to reduce the computational load on the avionics, the satellite's performance was tested with various CMOS sampling frequencies. Note that the Kalman filter rate is tied directly to the CMOS sampling frequency. Table 3 shows that the performance does not degrade significantly with slower sampling frequencies. Again, detection of Earth-sized exoplanets should still be possible at these lower rates.

Table 3: Fine jitter performance versus CMOS sampling frequency.

CMOS Sampling Freq. [Hz]	Fine $3\sigma$ Jitter [pixels]	Fine $3\sigma$ Jitter [arcsec]
4	0.09	3.3
8	0.06	2.2
12	0.05	1.8

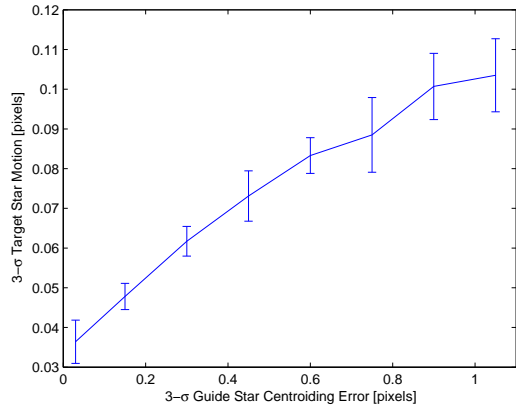


Figure 10: Target star motion versus guide star centroiding error.

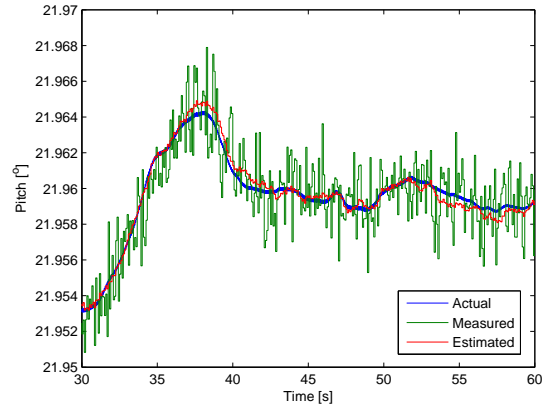


Figure 11: Kalman filter output for pitch axis with a  $3\sigma$  centroid error of 1.05 pixels.

### 4.3 Slew analysis

In addition to holding a certain attitude to a high level of precision, the ExoplanetSat must be able to slew to this attitude every orbit. To ensure that enough energy is gathered during orbit day and enough measurements are taken during orbit night, the time spent slewing should be minimized. Each of the reaction wheel types are analyzed for a worst-case slew maneuver. Note that the nominal reaction wheel speeds are set to 10% of the maximum wheel speed and the slew acceleration times are calculated so that only 60% of the reaction wheel momentum is used, leaving 30% as margin. Therefore, the time to slew is a function of both the maximum torque of the reaction wheels as well as the momentum storage capability.

Based on the current solar panel configuration (solar panels facing the opposite direction of the optics), the worst-case slew will occur during the time of year when the target star is closest to the sun. For Alpha Centauri B, this occurs in late November where the star and sun are approximately  $43^\circ$  apart. Observation of the target star may not be feasible during this time of year depending on the orbital parameters and the quality of the baffle used to shield the optics, but it will serve as the worst case for this analysis.

Figure 12 shows a representative slew maneuver from a sun-pointing attitude to a star-pointing attitude using the MAI-200 reaction wheel set. The first plot shows the eigenaxis slew from the sun-pointing attitude to the star-pointing attitude. From the second plot, it is clear that the satellite is following a smooth spinup-coast-spindown command profile. The third plot shows that the reaction wheels do not saturate due to the allotted 30% margin. Even though the planned slew maneuver takes only 45 seconds, it takes approximately an additional 35 seconds for the satellite to settle on the target star, as seen in Figure 13. This includes the time it takes to damp any residual satellite angular rates as well as lock onto the target star (the CMOS detectors are not used during fast maneuvers, hence attitude offsets may occur due to the biases and angle random walk of the gyroscopes).

This slew maneuver was performed with all the other candidate reaction wheels and the results are summarized in Table 4, showing both the slew maneuver time as well as total settling time. The other reaction wheel sets have much longer settling times due to the lower maximum torque and/or momentum storage capability. Interestingly, the RW 1 Type A and B models have a much lower additional settling time, since the angular rates of the satellite remain relatively low throughout the entire slew maneuver. From this table, it is clear that that MAI-200 is the best choice to minimize the slew time. In contrast, the RW 1 Type B is not a viable option since 61 minutes out of the 96-minute orbital period would be spent slewing, severely limiting the science measurements and solar energy gathered. Final selection of the reaction wheels will depend on a few other design considerations such as mass, volume, and power consumption.

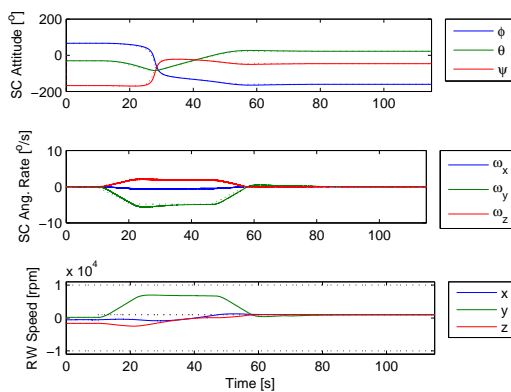


Figure 12: Slew maneuver using the MAI-200 reaction wheel set.

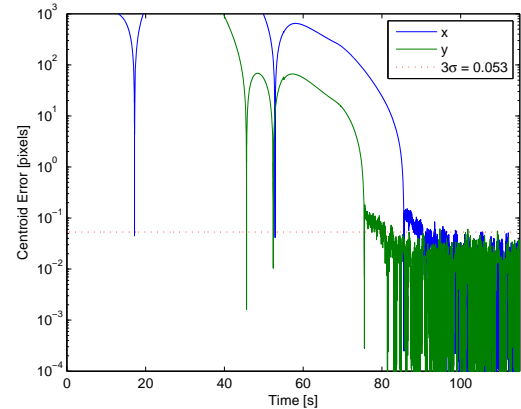


Figure 13: Target star centroid error versus time using the MAI-200 reaction wheel set.

Table 4: Slew settling time for various reaction wheels.

Reaction Wheel	Slew Maneuver Time [mm:ss]	Total Settling Time [mm:ss]
MAI-100	04:42	05:15
MAI-200	00:45	01:20
RW 1 Type A	06:15	06:45
RW 1 Type B	30:37	30:37

## 5. CONCLUSION

A detailed simulation of ExoplanetSat was developed to assess the feasibility of achieving high-precision pointing. This includes models of the satellite dynamics, actuators, sensors as well as software. This provided the capability to assess a few of the high-risk areas of the design such as reaction wheel disturbances, and centroid error as well as design choices such as reaction wheel selection.

The current simulation shows promising results. With a large overestimate of the static and dynamic imbalances of the reaction wheels, the satellite can hold the target star's centroid to within the same 0.05 pixels (equivalent to holding the cross-boresight attitude axes down to 1.8 arcseconds). Even if the baseline centroid error cannot be met or the CMOS sampling frequency needs to be reduced, performance has been shown to not degrade significantly. Slew performance has also been assessed, showing that the MAI-200 clearly gives the fastest slew and settling time. Other reaction wheels may be selected, however, based on other factors such as mass, volume, and power consumption.

While this initial analysis is encouraging, further work must be done to rigorously prove that ExoplanetSat is capable of achieving this high level of pointing precision. More detailed reaction wheel models are being developed to include additional harmonics and are being validated through further testing. This, coupled with a detailed modal frequency analysis of the structure, will provide wheel speed ranges that produce acceptable levels of jitter. In addition, a hardware-in-the-loop testbed is currently being developed to demonstrate the fine pointing capability of ExoplanetSat.

## APPENDIX A. BASELINE SIMULATION PARAMETERS

Category	Parameter	Variable	Value
Mission	Time of year	-	November 21, 2010
	Target star	-	Alpha Centauri B
Orbit	Altitude	-	600 km
	Inclination	-	0 degrees
Satellite	Inertia	$\mathbf{J}$	$\text{diag}([0.07 \ 0.07 \ 0.04]) \text{ kg}\cdot\text{m}^2$
	Drag coefficient	$c_{drag}$	2.5
Magnetorquer	Diffuse coefficient	$c_{diff}$	0.2
	Specular coefficient	$c_{spec}$	0.4
Piezoelectric stage	Max. dipole	-	0.03774 A·m <sup>2</sup>
	Quantization	-	8 bits
Reaction wheel	Max. position	-	100 $\mu\text{m}$
	Damping	$\zeta$	0.995
Optics	Bandwidth	$\omega_n$	10 Hz
	Process delay	-	0.1 s
CCD	Quantization	-	8 (MAI), 16 (RW 1) bits
	Focal length	$f$	85 mm
CMOS	Pixel size	-	15 $\mu\text{m}$
	Sampling frequency	-	12 Hz
Gyroscope	Pixel size	-	15 $\mu\text{m}$
	Centroid error	$E_{centroid}$	0.05 pixels
Magnetometer	Total pixels across CMOS detectors	$n_{pix}$	1024 pixels
	Number of guide stars	$n_{star}$	10 stars
Piezoelectric pos. sensors	Anti-aliasing	-	2 <sup>nd</sup> order elliptic filter
	Sampling frequency	-	200 Hz
Tachometer	Scale factor	-	100 ppm
	Angle random walk	-	0.01 $^\circ/\sqrt{\text{hr}}$
Control software	Bias instability	-	3.3 $^\circ/\text{hr}$
	Bias instability time constant	$\tau$	300 s
Navigation software	Saturation	-	30 $^\circ/\text{s}$
	Quantization	-	16 bits
Navigation software	Downsample filter	-	Running average
	Sampling frequency	-	4 Hz
Navigation software	Scale factor	-	25%
	Saturation	-	1100 $\mu\text{T}$
Navigation software	Quantization	-	0.015 $\mu\text{T}$
	Sampling frequency	-	12 Hz
Navigation software	Noise	-	0.3 nm
	Sampling frequency	-	4 Hz
Navigation software	Quantization	-	0.05 rpm
	Inertia uncertainty	-	4 Hz
Navigation software	Damping	$\zeta$	10%
	Bandwidth	$\omega_n$	0.995
Navigation software	Sampling frequency	-	0.04 Hz
			12 Hz

## ACKNOWLEDGMENTS

This work has been supported by the NASA Astrobiology Science and Technology Instrument Development (ASTID) Program.

## REFERENCES

- [1] M. W. Smith, S. Seager, C. M. Pong, J. S. Villaseñor, G. R. Ricker, D. W. Miller, M. E. Knapp, G. T. Farmer, and R. Jensen-Clem, "ExoplanetSat: Detecting and monitoring exoplanets using a low-cost, CubeSat platform," in *Proceedings of SPIE*, SPIE, (San Diego, CA), June-July 2010. Paper number 7731-78.
- [2] The CubeSat Program, California Polytechnic State University, San Luis Obispo, *CubeSat Design Specification*, August 2009. Revision 12.
- [3] P. H. Wirsching, T. L. Paez, and K. Ortiz, *Random Vibrations: Theory and Practice*, John Wiley & Sons Inc., New York, NY, 1 ed., 1995.
- [4] S. Lim, B. F. Lane, B. A. Moran, T. C. Henderson, and F. A. Geisel, "Model-Based Design and Implementation of Pointing and Tracking Systems: From Model to Code in One Step," in *33rd Annual AAS Guidance & Control Conference*, pp. 1–20, AAS, (Breckenridge, CO), February 2010. Paper number 10-036.
- [5] M. J. Sidi, *Spacecraft Dynamics and Control: A Practical Engineering Approach*, vol. 7 of *Cambridge Aerospace Series*, Cambridge University Press, New York, NY, 1997.
- [6] D. A. Vallado, *Fundamentals of Astrodynamics and Applications*, Space Technology Library, Microcosm Press and Springer, New York, NY, 3rd ed., 2007.
- [7] C. B. Spence, Jr., "Environmental Torques," in *Spacecraft Attitude Determination and Control*, J. R. Wertz, ed., ch. 17.2, D. Reidel Publishing Company, Boston, MA, 1978.
- [8] M. Plett, "Magnetic Field Models," in *Spacecraft Attitude Determination and Control*, J. R. Wertz, ed., ch. H, D. Reidel Publishing Company, Boston, MA, 1978.
- [9] "International Geomagnetic Reference Field." <http://www.ngdc.noaa.gov/IAGA/vmod/igrf.html>, January 2010.
- [10] *U.S. Standard Atmosphere 1976*, National Oceanic and Atmospheric Administration (NOAA), National Aeronautics and Space Administration (NASA), and United States Air Force (USAF), Washington, D.C., 1976.
- [11] B. Bialke, "High Fidelity Mathematical Modeling of Reaction Wheel Performance," *Advances in the Astronautical Sciences* **98**, pp. 483–496, 1998.
- [12] G. W. Neat, J. W. Melody, and B. J. Lurie, "Vibration Attenuation Approach for Spaceborne Optical Interferometers," *IEEE Transactions on Control Systems Technology* **6**, pp. 689–700, November 1998.
- [13] R. A. Masterson, D. W. Miller, and R. L. Grogan, "Development and Validation of Reaction Wheel Disturbance Models: Empirical Model," *Journal of Sound and Vibration* **249**(3), pp. 575–598, 2002.
- [14] K.-C. Liu, P. Maghami, and C. Blaurock, "Reaction Wheel Disturbance Modeling, Jitter Analysis, and Validation Tests for Solar Dynamics Observatory," in *AIAA Guidance, Navigation, and Control Conference and Exhibit*, pp. 1–18, AIAA, (Honolulu, HI), August 2008. Paper number 2008-7232.
- [15] C. C. Liebe, "Accuracy Performance of Star Trackers—A Tutorial," *IEEE Transactions on Aerospace and Electronic Systems* **38**, pp. 587–599, April 2002.
- [16] E. Lefferts, F. Markley, and M. Shuster, "Kalman Filtering for Spacecraft Attitude Estimation," *Journal of Guidance, Control, and Dynamics* **5**, pp. 417–429, September-October 1982.
- [17] B. Wie, H. Weiss, and A. Arapostathis, "A Quaternion Feedback Regulator for Spacecraft Eigenaxis Rotations," *Journal of Guidance, Control, and Dynamics* **12**(3), pp. 375–380, 1989.
- [18] IntelliTech Microsystems, Inc., Bowie, MD, *IMI-100 Miniature 3-Axis ADACS Product Specification*, October 2008. Presently Maryland Aerospace, Inc. in Crofton, MD.
- [19] IntelliTech Microsystems, Inc., Bowie, MD, *IMI-200 MiniADACS System Operations Manual*, July 2009. Rev. 7. Presently Maryland Aerospace, Inc. in Crofton, MD.
- [20] Astro- und Feinwerktechnik Adlershof GmbH, Berlin, Germany, *Reaction Wheel RW 1 for Pico and Nano Satellites*, February 2009.